Theory of Cytoskeletal Reorganization during Cross-Linker-Mediated Mitotic Spindle Assembly

Adam R. Lamson,[1] Christopher J. Edelmaier,[1] Matthew A. Glaser,[1] and Meredith D. Betterton[1,*]
[1]Department of Physics, University of Colorado, Boulder, Colorado

ABSTRACT Cells grow, move, and respond to outside stimuli by large-scale cytoskeletal reorganization. A prototypical example of cytoskeletal remodeling is mitotic spindle assembly, during which microtubules nucleate, undergo dynamic instability, bundle, and organize into a bipolar spindle. Key mechanisms of this process include regulated filament polymerization, cross-linking, and motor-protein activity. Remarkably, using passive cross-linkers, fission yeast can assemble a bipolar spindle in the absence of motor proteins. We develop a torque-balance model that describes this reorganization because of dynamic microtubule bundles, spindle-pole bodies, the nuclear envelope, and passive cross-linkers to predict spindle-assembly dynamics. We compare these results to those obtained with kinetic Monte Carlo-Brownian dynamics simulations, which include cross-linker-binding kinetics and other stochastic effects. Our results show that rapid cross-linker reorganization to microtubule overlaps facilitates cross-linker-driven spindle assembly, a testable prediction for future experiments. Combining these two modeling techniques, we illustrate a general method for studying cytoskeletal network reorganization.

INTRODUCTION

Cell survival depends on cells' ability to divide, grow, and respond to changing conditions, biological functions enabled by flexible and rapid remodeling of the cellular cytoskeleton. Cytoskeletal remodeling is essential for polarized growth, both of single cells (1,2) and tissues (3). During cell crawling and adhesion, turnover of the actin and microtubule (MT) cytoskeletons is tuned by signaling events (4,5). Large-scale cellular volume changes required for phagocytosis, exocytosis, and endocytosis require actin remodeling (6). Proper organization and localization of organelles, including mitochondria (7,8) and the endoplasmic reticulum (9), depend on dynamic interactions with the cytoskeleton. During mitosis and cytokinesis, the cytoskeleton undergoes large rearrangements to construct the mitotic spindle (10) and cytokinetic ring (6). Given the ubiquity of cytoskeletal remodeling for cellular behavior, it is not surprising that aberrant cytoskeletal dynamics or regulation are associated with many diseases, including cancer and developmental defects. The ability of the cytoskeleton to undergo rapid and large structural rearrangements is therefore of broad importance in biology.

The dynamic reorganization of cytoskeletal assemblies is facilitated by a small number of building blocks—filaments, molecular motors, cross-linkers, and associated proteins—which work in concert to generate force (4). Cytoskeletal filaments, including MTs and actin, undergo dynamic cycles of polymerization and depolymerization that allow rapid turnover. Filament nucleation is controlled by cellular factors (such as γ-tubulin for MTs (10) and the Arp2/3 complex for actin (6)), which spatiotemporally tune filament localization. Cross-linking proteins, including diverse actin cross-linkers (5,11) and the Ase1/PRC1/MAP65 family of MT cross-linkers (12–18), bundle cytoskeletal filaments to organize higher-order assemblies. These proteins can also have a preferred polarity for cross-linking parallel or anti-parallel filament pairs (5,13). Motor proteins such as kinesins and myosins can walk on filaments to transport cargo or cross-link and slide filaments to reorganize them (4). MT- and actin-binding proteins often regulate filament length and dynamics, allowing further control of cytoskeletal architecture (19–23). Although the flexible, dynamic nature of the cytoskeleton is essential for its biological function, we currently lack predictive understanding of cytoskeletal reorganization.

Biophysical modeling of cytoskeletal systems can reveal molecular mechanisms essential for self-assembly, give insight into the physical requirements for a given behavior, and be dissected in more detail than is possible

in experiments. For example, mathematical modeling has been used to study traveling waves of actin polymerization and protrusions in cell motility (24,25), cortical MT organization in plants (26–29), mitosis (30,31), and cytokinesis (32,33). A frontier in cytoskeletal modeling is the development of general methods to handle three-dimensional systems in which large structural rearrangements occur. Early mathematical modeling of the cytoskeleton focused on one-dimensional problems such as muscle contraction (34–36) and mitotic spindle length regulation (37–45). However, higher-dimensional models are required to capture significant rearrangements, such as the actin protrusions of motile cells, cytokinetic ring formation, and cell cleavage.

A prototypical example of cytoskeletal reorganization is mitotic spindle assembly, during which spindle MTs reorganize to form a bipolar structure as the spindle poles separate (Fig. 1) (46). This requires significant structural rearrangement in yeasts, which enter mitosis with side-by-side spindle-pole bodies (SPBs), the nucleating centers for spindle MTs (Fig. 1 B) (47,48). In the closed mitosis of yeasts, the SPBs are embedded in the nuclear envelope and therefore undergo constrained motion (49). Steric interactions between MTs, SPBs, and the nuclear envelope, along with fluid drag from the nucleoplasm, resist large-scale rearrangement of spindle components (50,51). Motor proteins and cross-linkers that bundle and slide MTs are key force generators for spindle assembly that create, extend, and stabilize MT bundles (13,17,40,47,48,50,52–62).

In contrast to the previously established importance of molecular motors in spindle assembly, recent work showed that fission-yeast spindles can assemble in the absence of mitotic motors if the passive cross-linking protein Ase1 is present (51,63). In most organisms, kinesin-5 motors that cross-link antiparallel MTs and slide them apart are essential for spindle-pole separation and the establishment of a bipolar spindle (47,48,52,64–70). Therefore, it was surprising that in fission yeast, kinesin-5 deletion mutants become viable when the kinesin-14s are simultaneously deleted and spindle assembly is rescued (53,71,72). In fact, spindle assembly can occur with all mitotic motors deleted or inhibited, and Ase1 is essential for spindle assembly in this context (51,63). In previous work, we developed a simulation model of spindle assembly both with (50) and without (51) motor proteins. In these simulations, antiparallel cross-linking by Ase1 and the stabilization of cross-linked MT dynamics are sufficient for model bipolar spindle assembly in the absence of motors (51). Related previous theory has studied mitotic MT bundling by motors and cross-linkers (73,74).

Here, we build on previous work to interrogate the requirements for cross-linker-mediated spindle assembly and characterize how varying properties of cross-linkers change spindle morphology. To the best of our knowledge, we develop a new theory to understand the minimal requirements for spindle structural reorganization and bipolar spindle assembly and make quantitative predictions for experiments. To describe the requirements for passive cross-linkers to align spindle MTs into a bipolar state, we developed a minimal model that accounts for rotation generated by MT polymerization, cross-linkers, drag, and steric
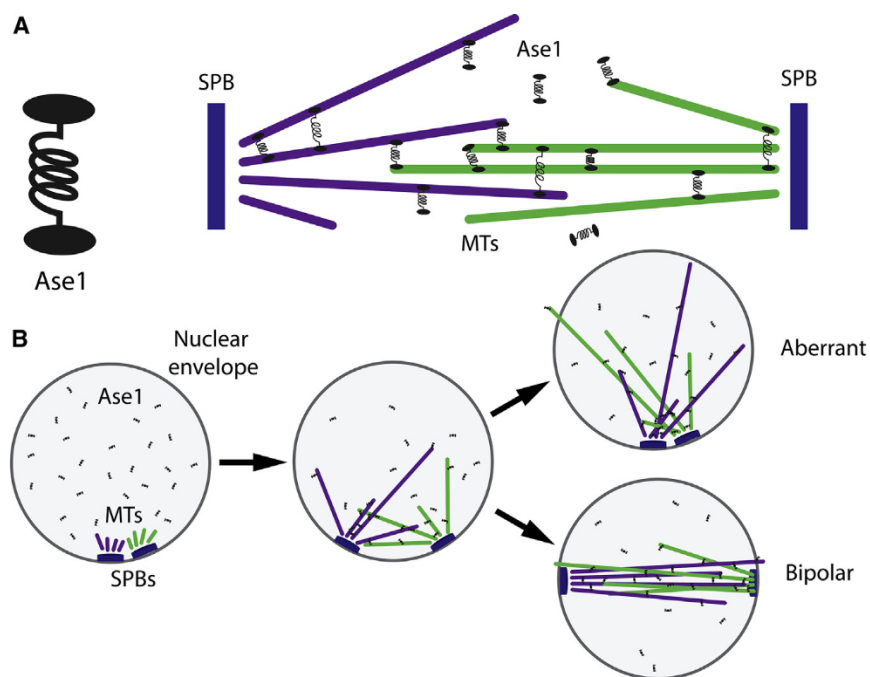

FIGURE 1 Schematic of spindle assembly by passive cross-linkers. (A) Ase1 cross-linker (left) and mitotic spindle (right), including spindle-pole bodies (SPBs, blue), MTs (purple and green), and Ase1 (black), are shown. (B) Steps of spindle assembly are shown starting from side-by-side SPBs (left), which leads to either a kinetically trapped aberrant state (right, top) or a bipolar spindle (right, bottom). To see this figure in color, go online.

interactions. We find that spindle assembly is sensitive to the initial angle at which MT bundles cross-link: a smaller initial angle and increased SPB separation facilitates spindle bipolarity. This leads to a geometric explanation of why spindles do not require extensile forces from motor proteins during assembly.

The model we develop includes the general features of dynamic cytoskeletal filaments, forces and torques generated by cross-linkers, friction, and steric interactions. Therefore, this torque-balance model can be applied generally to model cross-linked filament networks driven by polymerization dynamics, contraction, extension, and filament alignment.

METHODS

Minimal model of MT reorientation during spindle assembly

The forces and torques that drive cytoskeletal reorganization can be modeled and simulated using statistical mechanics and hydrodynamic drag. To create a predictive, tractable model of spindle assembly, we considered forces from interactions of MT bundles, SPBs, the nuclear envelope, and the nucleoplasm (Figs. 1 and 2; Fig. S1). MTs are nucleated by SPBs and subsequently bundled by passive cross-linkers. Although in principle multiple bundles may be nucleated from one SPB, there is typically one dominant bundle (75,76). SPBs are embedded in the nuclear envelope, which is roughly spherical and confines the SPBs to a position on that spherical shell. Motion of the SPB in the shell encounters a viscous drag (Fig. 2; Fig. S1). The shell prevents MT bundles and other elements of the nucleoplasm from exiting the nucleus. Nucleoplasmic viscosity pro-

duces a drag force that opposes the lateral motion of MT bundles and controls cross-linker diffusion (Fig. 2 A).

As an MT bundle grows, steric interactions with the nuclear envelope cause the bundle end to slide along the edge of the nucleus, which moves the bundle. We assume that the longest MT within the bundle touches the nuclear envelope and that MT ends slide freely along the surface of the nuclear envelope, neglecting friction in sliding studied previously (77–79).

Individual MTs undergo dynamic instability characterized by a polymerization speed v_p, depolymerization speed v_d, catastrophe frequency f_c, and rescue frequency f_r. In the bounded growth regime, these dynamic instability parameters lead to a decaying exponential distribution of MT length (80), which has been observed for some populations of spindle MTs (81). Consistent with this expectation, the measured dynamic instability parameters of single fission-yeast mitotic MTs were in the bounded growth regime (76), and therefore we used these parameters to model dynamics of single MTs in the full stochastic model (Table 1). However, cross-linked spindle MTs can be significantly stabilized, for example, by CLASP (57,82). As a result, bundled MT dynamics parameters may shift into the unbounded growth regime. Consistent with this hypothesis, the length distribution of midzone and kinetochore MTs in the spindle is nonexponential in several organisms (81,83–86). Because unbounded growth may occur in spatially confined regions such as the spindle midzone, we consider dynamic instability parameters in this regime for bundled MTs (Table 1). In the minimal torque-balance model of MT bundles, we neglect single-MT catastrophe and consider an average bundle growth speed v_{pavg} of

$$v_{pavg} = \frac{f_r v_p - f_c v_s}{f_r + f_c} > 0. \tag{1}$$

MT polymerization speed slows in response to compressive force along the MT axis, which we model as in previous work (Eq. S7) (87):

$$v_p(L) = \frac{v_o}{\eta - 1}\left(\eta^{1-L/2R} - 1\right), \tag{2}$$
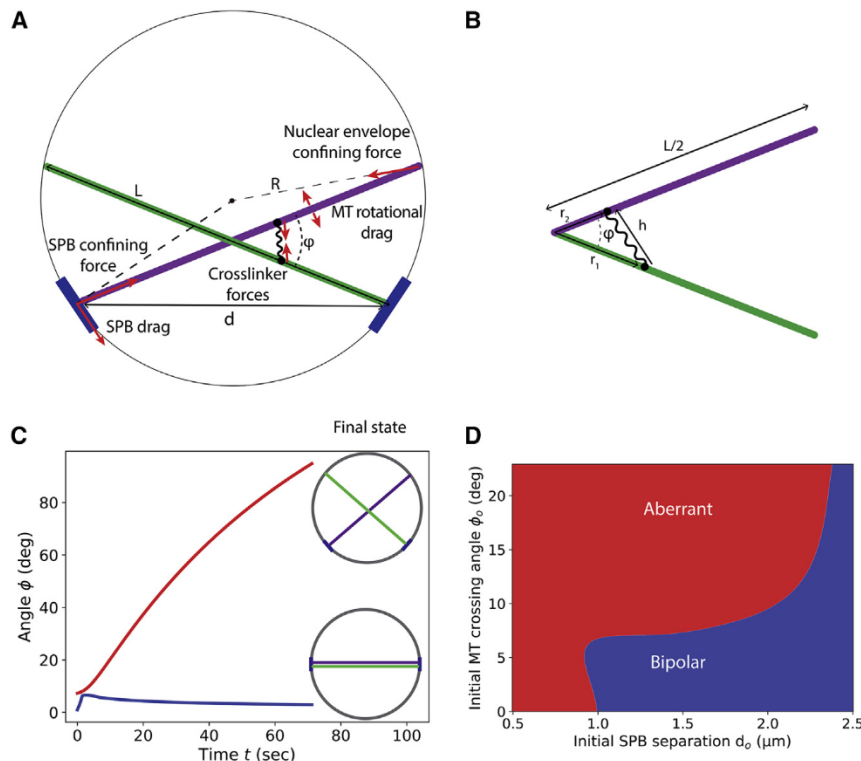
A **B**

C **D**

FIGURE 2 Schematic of and results from the torque-balance model. (*A*) A schematic of forces and torques is shown. MT bundles of length L are attached to SPBs, separated by distance d and crossing angle ϕ. Forces arise from cross-linkers, drag, and confinement within the nuclear envelope. (*B*) A schematic of cross-linking geometry is shown. Two MT bundles of length L cross at angle ϕ, with cross-linker heads binding at distance r_1 and r_2 from the MT bundle ends. (*C*) MT bundle cross-linking angle ϕ as a function of time in the torque-balance model is shown for two initial conditions. Red (*top*) larger initial crossing angle becomes larger, leading to an aberrant final state. Blue (*lower*) smaller initial crossing angle decreases, leading to an aligned bipolar spindle. (*D*) A phase diagram of bipolar spindle assembly in the torque-balance model as a function of initial SPB separation and crossing angle is shown. Blue, bipolar spindles form. Red, aberrant spindles form. Parameters are $v_p = 4$ μm/min, $h_{cl} = 53$ nm, $k_{cl} = 0.2055$ pN/nm, $R_{NE} = 1.375$ nm, $c_{cl} = 2.88 \times 10^{-4}$ nm^{-2}, $z = 1$, $d_o = 0.55$ μm, $D_{spb} = 4.5 \times 10^{-4}$ μm^2/s, initial angle $\phi_o = 6.07$ degrees for bipolar final state in (*C*), 9.1° for aberrant final state in (*C*). See Table 2. To see this figure in color, go online.

TABLE 1 MT, Nuclear Enevelope, and SPB Parameters Used in kMC-BD Model

Parameter	Symbol	Value	Notes
Nuclear envelope radius	R	1.375 μm	(75)
MT diameter	σ_{MT}	25 nm	(97)
MT angular diffusion coefficient	D_θ	Varies with MT length	(75)
Force-induced catastrophe constant	α_c	0.5 pN^{-1}	(87,98)
Membrane tube radius	f_{tube}	87.7 nm	(96,99)
Asymptotic wall force	f_w	2.5 pN	(96,99)
SPBs			
Diameter	σ_{SPB}	0.237 μm	(49)
Bridge size	N/A[a]	75 nm	(49)
Tether rest length	R_0	50 nm	(94,95)
Tether spring constant	K_0	0.67 pN nm^{-1}	typical value of protein spring constant, cf. (50)
Number of MTs per SPB	N_{MT}	14	(49)
Translational diffusion coefficient	D_t	4.5×10^{-4} m^2 s^{-1}	(50)
Rotational diffusion coefficient	$D_{\theta, spb}$	0.017 s^{-1}	(50)
Dynamic instability			
MT growth speed	$v_{g, 0}$	4 μm min^{-1}	(76)
MT shrinking speed	$v_{s, 0}$	6.7 μm min^{-1}	(76)
Catastrophe frequency	$f_{c, 0}$	6.07 min^{-1}	(76)
Rescue frequency	$f_{r, 0}$	0.71 min^{-1}	(51,76)
Growth speed stabilization	s_{vg}	1.5	Estimated based on model from (51)
Shrinking speed stabilization	s_{vs}	0.1	Estimated based on model from (51)
Catastrophe frequency stabilization	s_{fc}	0.1	Estimated based on model from (51)
Rescue frequency stabilization	s_{fr}	20	Estimated based on model from (51)
Stabilization length	s_ℓ	25 nm	Estimated based on model from (51)
Minimal MT length	L_{min}	50 nm	Value chosen for numerical stability
MT stall force	f_s	14.6 pN	(87)

For simulation details, see Supporting Materials and Methods.
[a]N/A, not applicable.

where $v_o = v_p(F_{w,\parallel} = 0)$ is the zero-force polymerization speed and the tubulin association constant $\eta = k_{\text{tubulin, on}}/k_{\text{tubulin, off}} = \exp(\delta F_s/k_B TN)$, where δ is the tubulin dimer length of 8 nm, F_s is the force at which MT polymerization stalls, $N = 13$ is the number of protofilaments in an MT, k_B is the Boltzmann constant, and T is the temperature (Table 2).

We assume perfectly rigid MTs, neglecting MT and bundle bending. The critical buckling force $F_c = EI/L^2$, where EI is the flexural rigidity of an MT and L its length. In our model, this force arises from the component of the wall force along the MT axis, $F_{w,\parallel} = F_s L/2R$, giving a critical buckling length for an MT of $L_c = (2REI/F_s)^{1/3}$. The flexural rigid-

ity $EI = 7.9$ pN μm^2 (88), and the nuclear diameter $2R = 2.75$ μm. If we consider the upper limit of the wall force as the MT growth stall force $F_s = 14.8$ pN, the critical length would be 1.14 μm, approximately the average length of unstabilized MTs (76). In practice, force-induced catastrophe of MTs causes MTs to transition to shrinking before reaching the buckling force. Further, in a multi-MT bundle, the buckling force greatly increases: for a hexagonal bundle of 14 MTs, each 2.75 μm long, the critical force is ~86 pN (41).

The nuclear envelope exerts equal and opposite radially inward forces on MT bundle ends, which produce a net force that moves the bundle center of mass toward the center of the nuclear envelope but produces no net torque

TABLE 2 Table of Parameter Values Used in the Torque-Balance Model

Parameter	Symbol	Value	Notes
Cross-linker spring constant	k_{cl}	0.2 pN nm^{-1}	(17)
Cross-linker length	h_{cl}	53 nm	(17)
Cross-linker fugacity	z_{cl}	1.0	chosen to have ~20 cross-linkers per MT at full overlap
Cross-linker binding affinity	c_{cl}	3×10^{-4} nm^{-2}	chosen to have ~20 cross-linkers per MT at full overlap
Nuclear envelope radius	R_{NE}	1.375 μm	(75)
Nucleoplasm viscosity	η_{nu}	10^3 cP	(50,75), Supporting Materials and Methods
SPB diffusion coefficient	D_{spb}	4×10^{-4} m^2 s^{-1}	(50)
MT stall force	$F^{\text{stall, MT}}$	14.8 pN	(87)
MT polymerization rate	v_o	4 μm min^{-1}	range 0.5–10.0 μm min^{-1} (75,76)
Time step	δt	0.0358 s	chosen for numerical stability

For details, see Supporting Materials and Methods.

(Fig. S1 B). MT bundle minus ends interact with SPBs; this coupling to SPBs with their large drag breaks the symmetry between plus and minus ends and produces a net torque about the bundle centers. SPB drag on the minus ends of MT bundles tends to rotate the bundles away from alignment, leading to a torque

$$\tau_{\text{spb}}(\dot{\phi}, L) = -\gamma_{\text{spb}} \frac{L}{4} \left(\dot{\phi} \sqrt{R^2 - (L/2)^2} - \dot{L} \right), \quad (3)$$

where γ_{spb} is the friction coefficient of SPBs, R is the radius of the nuclear envelope, ϕ is the bundle crossing angle, and $\dot{\phi}$ is the time derivative of ϕ (Fig. 2 A; Fig. S1 A). The magnitude of the SPB torque τ_{spb} is proportional to γ_{spb}, the MT bundle polymerization speed $\dot{L}$, and bundle length L (Eq. S13). However, longer MTs experience a greater parallel force (along the MT axis) from the nuclear envelope than perpendicular force (perpendicular to the MT axis), which slows MT polymerization, reduces SPB velocity, and therefore lowers the antialigning torque (Fig. S1).

We calculate the average force and torque exerted by cross-linkers on MT bundles by considering the statistical mechanics of cross-linker binding, unbinding, stretching, and compression. Because cross-linker binding and unbinding kinetics are relatively fast (timescale of seconds) compared to spindle assembly (timescale of minutes), we make a quasi-steady-state assumption that cross-linker binding equilibrates given the instantaneous MT bundle positions. Therefore, we can determine cross-linker-induced forces and torques on MTs by computing the grand partition function and its derivatives. This approach is computationally inexpensive compared to calculation of single-particle dynamics. Calculating forces and torques through the cross-linker partition function may be applied generally to filament networks with fast rearrangement of passive cross-linkers compared to the movement of filaments.

The single-cross-link partition function between two filaments is the integral of the Boltzmann factor $e^{\beta u_{\text{cl}}}$, where u_{cl} is the cross-linker binding free energy, over all possible binding configurations (50,51)

$$q(\phi, L) = c \int_0^{L/2} \int_0^{L/2} dr_1 dr_2 e^{-\frac{\beta k}{2}(h(r_1, r_2, \phi) - h_{\text{cl}})^2}, \quad (4)$$

where c is the cross-linker concentration; the integrals over cross-linker endpoints r_1, r_2 extend over half the filament length from 0 to $L/2$; k is the cross-linker spring constant; ϕ is the angle between the two filaments; $h(r_1, r_2, \phi) = \sqrt{r_1^2 + r_2^2 - 2r_1 r_2 \cos(\phi)}$ is the cross-linker length when the endpoints are at r_1 and r_2 along the two filaments; h_{cl} is the cross-linker rest length (at which it is neither stretched nor compressed); and $\beta = 1/(k_B T)$ is the inverse temperature (Fig. 2 B; Eq. S17). We assume that cross-linkers do not interact with each other, which motivates the use of the grand canonical ensemble of a noninteracting gas with partition function

$$\Xi = \sum_{n=0}^{\infty} \frac{1}{n!} z^n q^n = e^{zq}. \quad (5)$$

Here, n is the number of bound cross-linkers and z is the fugacity $e^{\mu_{o,\text{cl}}\beta}$, where $\mu_{o,\text{cl}}$ is the chemical potential of cross-linkers binding to the filaments. We can then determine cross-linker force and torque from derivatives of the grand potential

$$\Phi = \frac{-1}{\beta} \ln(\Xi) = \frac{-zq}{\beta}. \quad (6)$$

For example, the torque from all cross-linkers on MT bundles is

$$\tau(\phi, L) = -\frac{\partial \Phi}{\partial \varphi} = -zck\sin(\phi) \int_0^{L/2} \int_0^{L/2} dr_1 dr_2 r_1 r_2$$
$$\times \left(1 - \frac{h_{cl}}{h(r_1, r_2, \phi)} \right) e^{-\frac{\beta k}{2}(h(r_1, r_2, \phi) - h_{\text{cl}})^2}. \quad (7)$$

Torque due to cross-linkers can promote or oppose antiparallel alignment of MTs because the magnitude and direction of the torque depends on MT length and the crossing angle (Fig. 2). Cross-linkers can bind above, below, to the left, and to the right of the crossing point. Symmetry allows us to consider only the left-right and above-below cases: the angle in Eq. 7 is ϕ for left-right and $\pi - \phi$ for above-below. As expected, a small angle between bundles produces greater cross-linker attachment and therefore greater torque. Left-right binding typically produces aligning torque, although there can be exceptions when the cross-linkers are too compressed upon binding.

By using the Langevin equations for translational and rotational motion of filaments, we can derive a system of integro-differential equations for ϕ and L (Supporting Materials and Methods, Section S1, Eqs. S2 and S22)

$$\dot{\phi}(\dot{L}, L, \phi, t) = \frac{\gamma_{\text{spb}} L \dot{L} + 2\tau_{\text{cl},-} - 2\tau_{\text{cl},+}}{2\gamma_{\text{rot}} + \gamma_{\text{spb}} L \sqrt{R^2 - (L/2)^2}}, \quad (8)$$

$$\dot{L}(L, t) = v_p(L), \quad (9)$$

where $\gamma_{\text{rot}}(L)$ is the rotational drag coefficient of a filament of length L (89). These equations can be solved numerically given initial ϕ_0 and d_0 (Fig. 2 A; Eq. S2). The time evolution predicts the end configuration, either bipolar or aberrant (Fig. 2 C; Supporting Materials and Methods, Section S1.1).

RESULTS AND DISCUSSION

Phase diagram of spindle assembly

To compute a phase diagram for spindle assembly as a function of initial conditions, we numerically integrated Eqs. 8 and 9 (Supporting Materials and Methods). Dynamics that reach a bipolar final state have a decreasing crossing angle ϕ at the end of the integration, $d\phi/dt < 0$ (Fig. 2 C; Figs. S2–S4). Aberrant states occur for a larger initial crossing angle because the aligning torque from cross-linkers is not able to overcome the antialigning torque from SPB drag (Fig. 2 D). For larger SPB separation, longer MTs provide more sites for cross-linker binding, whereas steric forces from the nuclear envelope are more parallel to the MT axis, slowing polymerization and reducing SPB drag. For MTs that span the nucleus, bipolarity occurs whenever $\phi_o < \pi/2$ because the cross-linker aligning torque dominates. In fission-yeast spindle assembly, bundles tend to cross-link initially at short SPB separation (90). Our results show that model parameters that favor bipolarity for small SPB separation will favor spindle assembly for a range of initial conditions. This result is sensitive to the MT polymerization rate: slower MT polymerization decreases the torque

from SPBs, increasing the range over which spindles can become bipolar (Fig. S5).

Comparison to kinetic Monte Carlo-Brownian dynamics simulations

Our kinetic Monte Carlo-Brownian dynamics (kMC-BD) simulation model includes three-dimensional geometry, multiple sterically interacting MTs, and stochastic effects (50,51), making it a useful point of comparison with the minimal torque-balance model (Fig. 3; Video S1). In contrast to the torque-balance model, kMC-BD simulations with the same parameters do not always end in the same state because of stochastic effects, including thermal motion, randomly generated MT nucleation sites and initial cross-linker location, and binding kinetics. These stochastic effects also allow spindles to escape aberrant states and become bipolar (Fig. 3 B). The three-dimensional geometry adds another degree of freedom, increasing the number of ways to escape from kinetic traps.

In our kMC-BD model, the total cross-linker number is fixed, and we compute the location of individual molecules, which allows cross-linker forces to fluctuate (Table 3). Therefore, the overall force that cross-linkers can exert is constrained by the total cross-linker number. Cross-linkers must diffuse or unbind and rebind to apply force to recently overlapped MTs, processes that are modulated by thermal fluctuations, force, and MT configuration. The kMC-BD model becomes more similar to the quasisteady approximation used in the torque-balance model for high cross-linker turnover and/or high bound diffusion coefficient. Unlike in the torque-balance model, the distribution of cross-linkers can be out of equilibrium because small random thermal movements of MTs and SPBs occur on short timescales compared to the redistribution of cross-linkers. Out of equilibrium, cross-linkers exert restoring forces that maintain the network configuration despite random forces acting on MTs and SPBs. The stochastic binding kinetics allow

kMC-BD simulations to escape kinetic traps, but, if rearrangement is too slow compared to thermal motion, nonequilibrium effects can increase the strength of kinetic traps and the frequency of aberrant states. We quantified spindle assembly frequency as the fraction of simulations that end in a stable bipolar state after 24 min of simulated real time (51). A higher spindle-assembly frequency occurs in the phase diagram of the kMC-BD model (Fig. 3 C) for parameter sets that give bipolar spindle assembly in the torque-balance model (Fig. 2 D), demonstrating that the torque-balance model contains the key ingredients that control bipolar spindle assembly in the full kMC-BD model. The differences between these predictions highlight the importance of stochastic effects and cross-linker rearrangements in spindle assembly.

Lengthening cross-linkers inhibits bipolar spindle assembly by overbundling parallel MTs

Cross-linkers have a characteristic length, but it is not well understood whether changes in this length might affect spindle assembly. We assume Ase1 is around 40–55 nm long, based on the length of the human homolog PRC1 (37 nm long (91)) and kinesin-5 cross-linking motors (53 nm long (92)). In our model, cross-linkers are springs so that stretched cross-linkers pull MTs together, whereas compressed cross-linkers push them apart. Cross-linker length determines the distance from the MT crossing point at which cross-linkers prefer to bind, which affects the amount of splay in MT bundles.

Short cross-linkers inhibit spindle assembly because cross-linkers primarily bundle neighboring MTs, limiting interdigitation of antiparallel MTs (Fig. 4; Video S2). MT bundles become tightly bound and are less likely to become interdigitated with MTs from the other SPB, which decreases the strength of the cross-linker aligning torque (Fig. 4 A, *bottom left inset*).
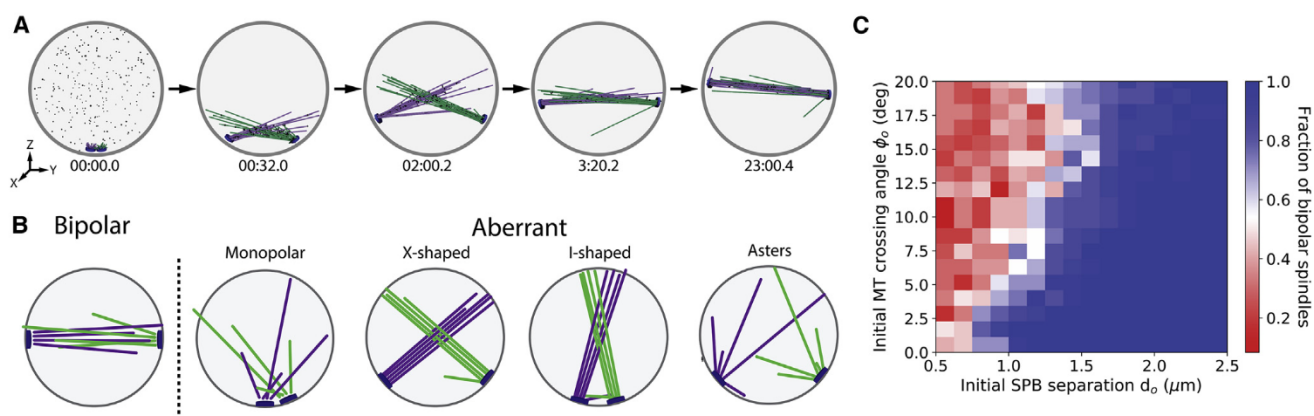

FIGURE 3 kMC-BD simulation snapshots, typical final states of simulations, and phase diagram. (*A*) Simulation snapshots of bipolar spindle assembly from an initial condition with adjacent SPBs are shown. Times shown are in minutes, seconds, and tenths of seconds. (*B*) Schematics of final states of simulations are shown. (*C*) A phase diagram of spindle formation failure is shown: red indicates an aberrant end state, blue the formation of a bipolar structure. Bipolar spindle fraction is determined from 24 simulations at each data point. See Video S1. To see this figure in color, go online.

TABLE 3 Passive Cross-Linker Parameters Used in kMC-BD Model

Parameter	Symbol	Value	Notes
Available molecules	N_{tot}	250	(100)
One-dimensional effective concentration	$c_{c, 2}$	0.4 nm^{-1}	(17)
Spring constant	K_c	0.2047 pN nm^{-1}	(17)
Diffusion constant (solution)	D_{free}	4.5 μm^2 s^{-1}	(101)
Singly bound diffusion constant	D_{sb}	0.1 μm^2 s^{-1}	(17)
Doubly bound diffusion constant	D_{db}	0.0067 μm^2 s^{-1}	same as the singly bound hopping rate (50)
Singly bound off rate	k_1	0.1 s^{-1}	(102)
Doubly bound off rate	k_2	0.05 s^{-1}	(17)
Parallel/antiparallel binding ratio	α	1/3	(102)
Unbinding load sensitivity	λ	0.01626	(50)

For details, see Supporting Materials and Methods.

Increasing cross-linker length too far allows cross-linkers to interact with more MTs, which negatively impacts spindle assembly in two ways: cross-linking occurs when the SPB separation is small, and MT bundles form aberrant I- and X-shaped spindles (Fig. 3 B). Longer cross-linkers splay parallel bundles, limiting MT cross-linking near the dynamic ends of the bundles. Cross-linking between splayed bundles tends to trap the SPBs close together, leading to a narrow X- or I-shaped spindle (Fig. 4 A, insets; Video S2). These effects make I- and X-shaped spindles strong kinetic traps for long cross-linkers.

These results suggested that the defects of the model with long cross-linkers might be rescued by separating SPBs at the start of the simulation. To test this prediction, we began simulations with SPBs separated and allowed MTs and cross-linkers to interact while the SPBs were held in place for 1 s. Spindle-assembly frequency increases sharply as

initial SPB separation increases above around 1.2 μm, similar to the location of the phase boundary in our torque-balance model (Fig. 4, B and C).

Increased cross-linker turnover helps spindles escape kinetically trapped aberrant states

Because in previous work, we found that cross-linker-only simulated spindles can become stuck in persistent monopolar states (51), we tested whether more rapid cross-linker turnover can promote bipolar spindle assembly by accelerating escape from aberrant states (Fig. 5; Video S3). Increasing turnover does not alter the average number of bound cross-linkers but increases binding and unbinding (between one- and two-head bound states). With increased turnover, stretched or compressed cross-linkers more rapidly detach and can rebind in states closer to mechanical equilibrium of
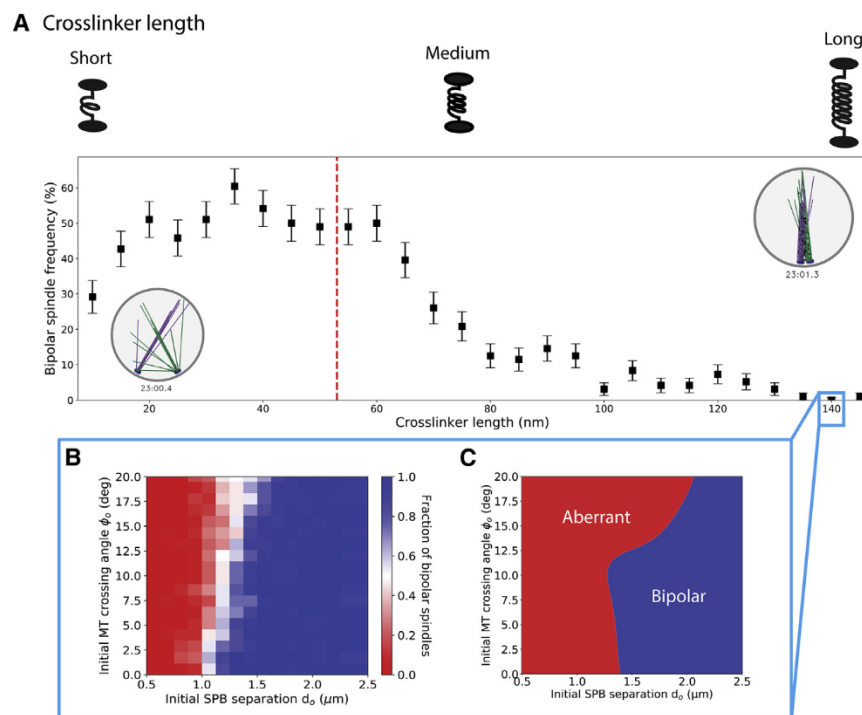

FIGURE 4 Cross-linker length of 20–60 nm is optimal for spindle assembly. (A) Fraction of simulations that assemble a bipolar spindle as a function of cross-linker length are shown. Top is a schematic of cross-linker length effects. Inset is simulation snapshots of typical aberrant final states. Red dotted line indicates reference parameter value. (B and C) Effects of long cross-linkers on spindle assembly for cross-linkers 140 nm long are shown. (B) The fraction of simulations that assemble a bipolar spindle as a function of initial SPB separation is shown. (C) A spindle-assembly phase diagram from the torque-balance model with long cross-linkers is shown. See Video S2. Error bars were calculated from the standard error of a binomial distribution. To see this figure in color, go online.
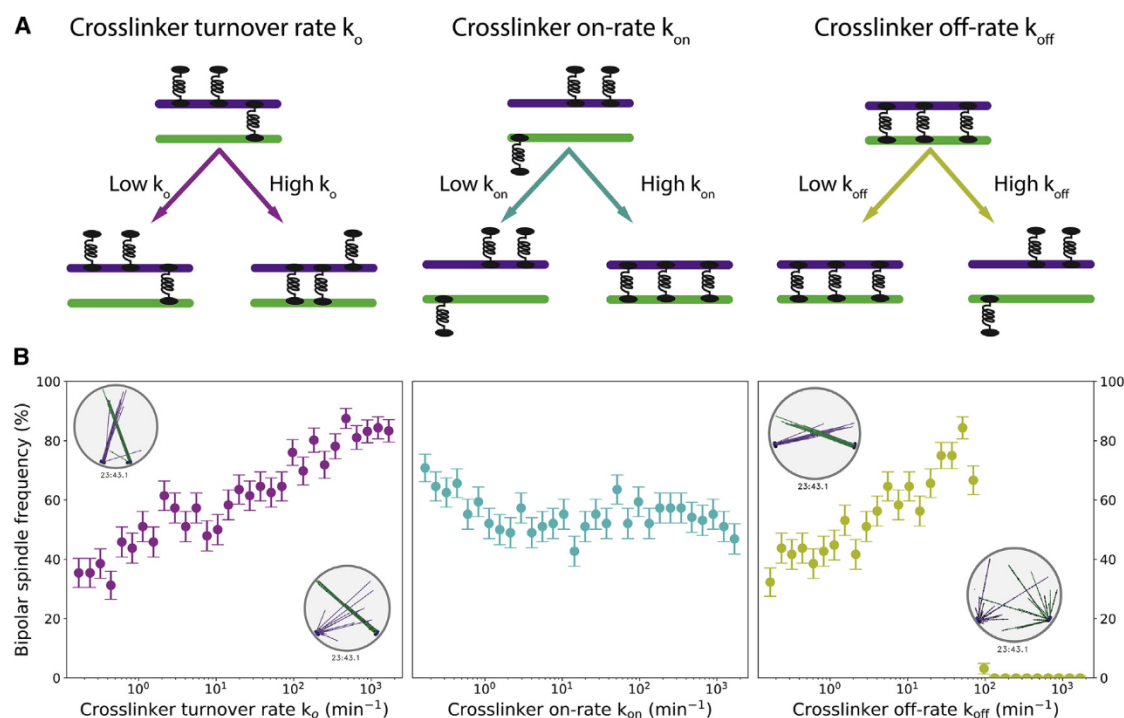
FIGURE 5 High cross-linker turnover facilitates spindle assembly. (*A*) Schematic effects of varying cross-linker kinetic rates are shown. Changing turnover (*left*) changes both on and off rates for transitions between one and two heads bound. Changing the on rate (*center*) changes the binding rate from one head to two. Changing the off rate (*right*) changes the unbinding rate from two heads to one. (*B*) The fraction of simulations that assemble a bipolar spindle as a function of cross-linker kinetic rates is shown. See Video S3. To see this figure in color, go online.

the spring. Rapid turnover therefore makes random thermal forces more effective at repositioning MT bundles.

Similar to increasing the turnover rate, increasing the unbinding rate of doubly bound cross-linkers facilitates the transition to a bipolar spindle by accelerating bundle reconfiguration. However, increasing the unbinding rate too much decreases the average number of cross-links, leading to a critical value of unbinding rate above which the number of bound cross-linkers is too low to maintain bundle integrity (Fig. 5 *B*; Video S3).

When cross-linker turnover is rapid, the kMC-BD simulation model more closely approximates the torque-balance model's quasisteady binding approximation. In this limit, cross-linkers rapidly change their configuration to the most statistically probable. In this case, we expect that fluctuations and aligning torque from cross-linkers will allow X-shaped spindles to form a bipolar spindle, given sufficient time. Although not every simulated spindle reaches a bipolar state with high cross-linker turnover, the trends match this expectation.

Cross-linker diffusion facilitates escape from kinetic traps by promoting cross-linker redistribution and MT reorientation

One-dimensional diffusion of bound cross-linkers repositions cross-linker heads on MTs, which suggests that a higher diffusion coefficient might promote escape from aberrant states. Because diffusion is biased by force, when random thermal forces reorient MTs and extend or compress the cross-linkers, diffusion favors cross-linker motion that reduces this force. Therefore, diffusion modulates MT structural rearrangement: slow diffusion tends to inhibit MT reorientation, whereas fast diffusion tends to promote it (Fig. 6; Video S4).

Increasing the doubly bound diffusion coefficient promotes spindle assembly, similar to the effects of increased turnover, but there are some differences. An increased diffusion coefficient by itself does not release cross-linked MTs and so does not lead to the separated asters seen for high cross-linker unbinding rate. In the opposite limit, when we completely remove doubly bound cross-linker diffusion, bipolar spindles do not form because cross-linkers do not rearrange quickly enough. Instead, these simulations produce long-lived I- or X-shaped spindles. In I-shaped spindles, the cross-linked bundles remain close together because cross-linkers cannot migrate when SPBs fluctuate apart.

The similar increases in spindle-assembly frequency for increasing turnover and diffusion suggest that changing turnover might be able to rescue the absence of diffusion: if binding kinetics are sufficiently rapid, one head can unbind and reattach in a different position, redistributing the cross-linkers. Consistent with this, high turnover rescues spindle assembly in simulations lacking bound diffusion
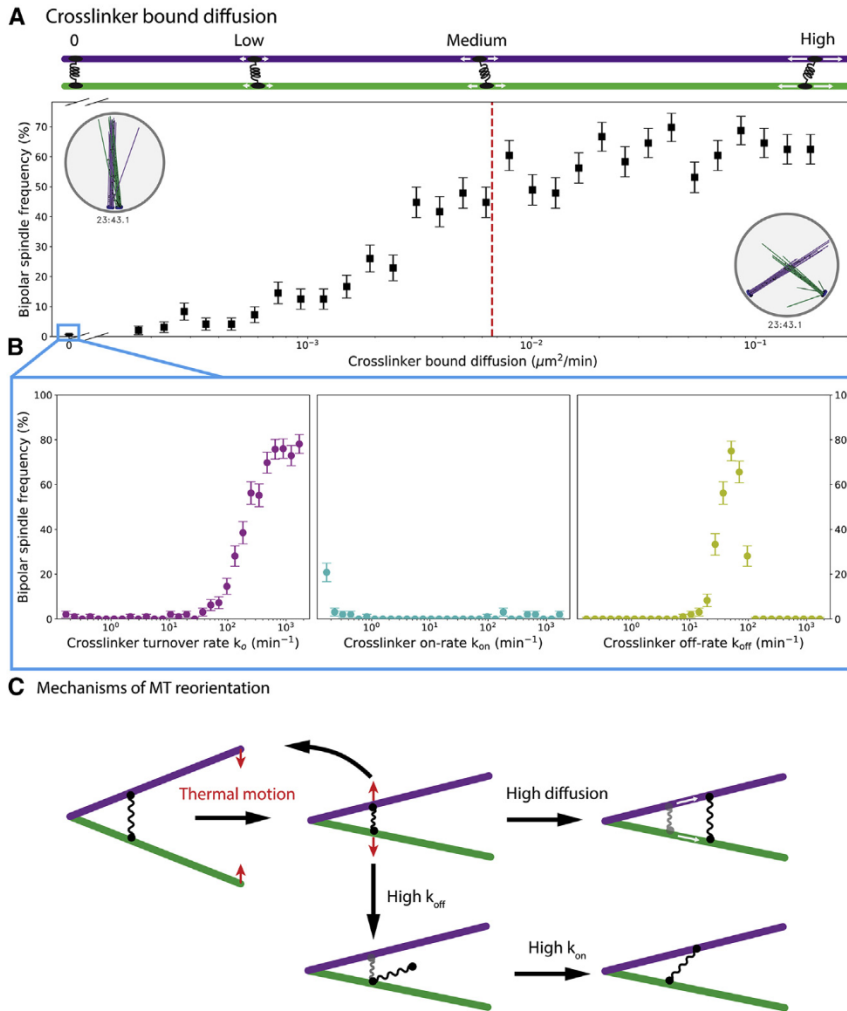
FIGURE 6 Bound cross-linker diffusion facilitates cross-linker redistribution and spindle assembly. (*A*) The fraction of simulations that assemble a bipolar spindle as a function of bound cross-linker diffusion coefficient is shown. Red dotted line indicates reference parameter value. Top is a schematic of bound diffusion coefficient effects. Inset shows simulation snapshots of typical aberrant final states. (*B*) The fraction of simulations that assemble a bipolar spindle as a function of cross-linker kinetic rates in the absence of bound cross-linker diffusion is shown. Bipolar spindle formation is rescued by high cross-linker turnover. (*C*) A schematic showing how high cross-linker turnover can rescue MT reorientation in the absence of bound diffusion is given. See Video S4. To see this figure in color, go online.

(Fig. 6 *B*). Similarly, a high cross-linker unbinding rate can rescue spindle bipolarity for a narrow range of values before reaching the critical value at which too few cross-linkers remain bound.

Bipolar spindles form most readily when the parallel/antiparallel binding ratio is low but nonzero

Cross-linkers of the Ase1/PRC1/MAP65 family have a binding preference for antiparallel MT overlaps (14,15,93), but it has not been determined whether this bias affects cross-linker-mediated bipolar spindle assembly. Previous work has found that cross-linkers in this family favor antiparallel MT binding over parallel by a factor of 2–10 (13). In our model, we implement this effect as a binding enhancement that changes when the angle between MT axes is greater or less than 90°. We then examined whether varying this binding preference affects spindle assembly (Fig. 7).

For low parallel/antiparallel binding ratio ($\alpha = 0$–0.01), spindles can form because cross-linkers inhibited in parallel bundling avoid the X-shaped spindle. In this limit, failure of bipolar spindle assembly occurs sometimes because antiparallel bundling for very short MTs from adjacent SPBs leads to trapped monopolar spindles (Fig. 7; Video S5). Parallel cross-linking can promote spindle assembly by forming X-shaped spindles that allow the SPBs to separate, then interdigitate.

For low-intermediate parallel/antiparallel binding ratio ($\alpha = 0.01$–0.1), predominantly antiparallel binding with some parallel binding allows X-shaped spindles to transition to bipolar spindles, leading to the highest frequency of spindle assembly observed. Monopolar spindles tend to be short-lived because parallel binding allows cross-linkers to migrate away from short antiparallel overlaps, promoting SPB separation (Fig. 7 *C*; Video S5). Bundles then either break up to form a bipolar spindle or rotate until the bundles are antiparallel.

For larger parallel/antiparallel binding ratio ($\alpha = 0.1$–0.3), the modest increase in parallel cross-linking favors

A Parallel-to-antiparallel binding ratio

B

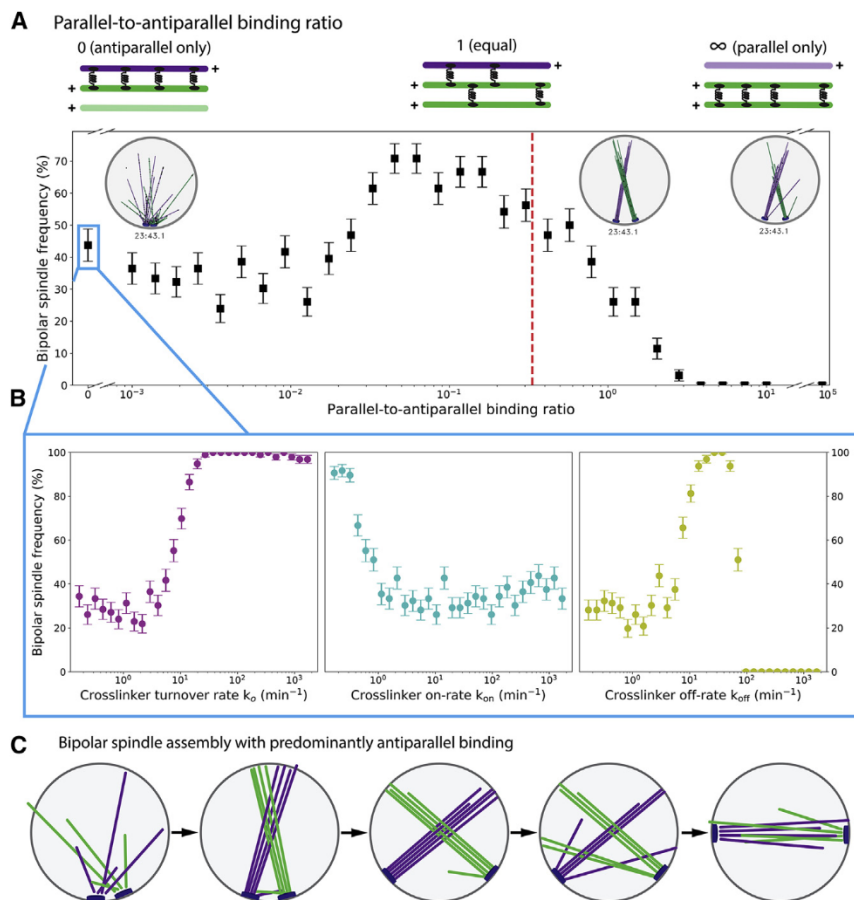**C** Bipolar spindle assembly with predominantly antiparallel binding

FIGURE 7 The cross-linker binding preference for antiparallel MTs promotes spindle assembly. (*A*) The fraction of simulations that assemble a bipolar spindle as a function of the parallel/antiparallel binding ratio α is shown. The red dotted line indicates the reference parameter value. Top is a schematic of binding ratio effects. Inset shows simulation snapshots of typical aberrant final states. (*B*) The fraction of simulations that assemble a bipolar spindle as a function of cross-linker kinetic rates in the absence of parallel binding is shown. (*C*) A schematic of the spindle-assembly pathway for the optimal binding ratio is shown. MTs cross-link parallel bundles, SPBs separate, and then bundles interdigitate at a shallower angle to form a bipolar spindle. See Video S5. To see this figure in color, go online.

the X-shaped spindle, inhibiting bipolarity. The lifetime of the X-shaped spindle increases with α. Similarly, when parallel and antiparallel binding are equally likely ($\alpha = 1$), X-shaped spindles typically form. However, random thermal forces can occasionally lower the angle between bundles, allowing antiparallel cross-links and a bipolar spindle to form. Fully extended bundles at right angles to each other have, on average, balanced torques promoting alignment and antialignment. This balance can be broken if a thermal fluctuation rotates bundles toward antiparallel alignment.

For purely antiparallel binding ($\alpha = 0$), increasing cross-linker turnover has a dramatic effect (Fig. 7 *B*). If turnover is sufficiently high, purely antiparallel-binding cross-linkers produce bipolar spindles for nearly every simulation. Varying turnover and unbinding rate show similar trends, except for the failure above the critical value for the unbinding rate at which most cross-linkers unbind. As for the other model perturbations discussed above, rapid rearrangement of cross-linkers allows spindles to escape kinetic traps and become bipolar.

Spindles typically transition from X-shaped to bipolar via two pathways: reconfiguration of cross-linkers and aligning torques between bundled MTs (Fig. 7 *C*; Video S5). Slow reconfiguration occurs when MT bundles move into antipar-

allel alignment because of thermal motion and cross-linker torque. The aligning torque pathway occurs more often when α is small so that single polar MTs are common. When single MTs escape the main bundles, they can cross-link with MTs from the other SPB at a relatively shallow angle. This allows the MTs to push against the nuclear envelope and separate SPBs until the main MT bundles also align into a fully bipolar spindle.

CONCLUSIONS

Here, we have developed a physical theory of cytoskeletal reorganization during fission-yeast mitotic spindle assembly (Fig. 1) that incorporates the key ingredients of filament polymerization and depolymerization, cross-linking, steric interactions, and drag (Fig. 2). Comparison of our minimal torque-balance model to full kMC-BD simulations that incorporate all stochastic effects (Fig. 3; Video S1) shows good agreement, demonstrating that the torque-balance model can illuminate the physical constraints on cross-linker-mediated spindle assembly. We studied specific individual perturbations to cross-linker length (Fig. 4; Video S2), binding kinetics (Fig. 5; Video S3), bound diffusion (Fig. 6; Video S4), and parallel versus antiparallel binding

preference (Fig. 7; Video S5). The results demonstrate that cross-linkers that favor binding to antiparallel MT pairs and rapid redistribution of cross-linkers are crucial for bipolar spindle assembly from initially side-by-side SPBs.

In cross-linker-mediated spindle assembly, the cross-linker binding preference to antiparallel rather than parallel MT pairs is important for spindle assembly: bipolar spindles have more possible binding states between antiparallel MT pairs, so the antiparallel binding preference energetically favors bipolarity. However, this state must still be kinetically reachable from an initial condition in which spindle MTs are predominantly parallel. Therefore, cross-linker-mediated spindle assembly is vulnerable to kinetic traps at key stages of assembly (Fig. 3). If antiparallel cross-linking predominates when SPBs are close to each other and cross-linker redistribution is too slow, spindles become trapped in a monopolar state. If parallel cross-linking predominates and cross-linkers either cannot bind to antiparallel MTs or redistribute too slowly, the frozen parallel bundles of X- or I-shaped spindles predominate. If too few cross-linkers are present, the spindle can fall apart into separated asters.

We further examined whether changing the binding and unbinding rates (Figs. 5 A and 7 B) individually has similar effects. Increasing the on rate tends to lock in monopolar states because it increases the total number of bound cross-linkers. For a high binding rate, nearly all cross-linkers are bound to two MTs, preventing them from reorienting. By contrast, for a low binding rate, cross-linkers can remain with one head bound to an MT while they diffuse, then reform a cross-link at another position. Our results therefore suggest that the rate of cross-linker rearrangement controls the rate of MT rearrangement and thus the rate of bipolar spindle assembly.

Spindles avoid or escape kinetic traps when aligning torques overcome antialigning torques early in spindle assembly. The torque-balance model demonstrates that aligning torques are strongest for separated SPBs and low crossing angle between MTs. In some cases, aligning torques must overcome the antialigning torques early in our model simulations if the spindle is to become bipolar. Important stochastic effects that promote escape from kinetic traps include cross-linker redistribution and random thermal forces. Cross-linker redistribution is faster when cross-linker binding kinetics and/or bound diffusion are more rapid. Remarkably, increasing cross-linker turnover or diffusion can rescue defects in bipolar spindle assembly caused by cross-linkers of nonoptimal length or exclusively antiparallel cross-linker binding.

The modeling techniques we use are generally applicable to cytoskeletal reorganization in which cross-linkers facilitate reorientation of filaments. This area is a frontier of cytoskeletal theory and modeling as the field confronts more challenging three-dimensional problems. Despite the complex dynamics and large-scale filament rearrangements that occur during bipolar spindle assembly, our work shows that the key physical effects can be understood both in detailed simulations and a minimal torque-balance model. The principles and modeling methods we describe are broadly applicable to cytoskeletal systems.

All data and computer code for this study are available on request from the atuhors.

SUPPORTING MATERIAL

AUTHOR CONTRIBUTIONS

A.R.L., M.A.G., and M.D.B. formulated the torque-balance model and code. A.R.L., C.J.E., and M.A.G. wrote the kMC-BD simulation code. A.R.L. ran kMC-BD simulations. A.R.L., C.J.E., and M.D.B. analyzed model results. A.R.L. and M.D.B. drafted the manuscript. A.R.L., C.J.E., M.A.G., and M.D.B. edited the manuscript.

ACKNOWLEDGMENTS

REFERENCES

1. Nelson, W. J. 2003. Adaptation of core mechanisms to generate cell polarity. *Nature.* 422:766–774.

2. Fischer, R., N. Zekert, and N. Takeshita. 2008. Polarized growth in fungi–interplay between the cytoskeleton, positional markers and membrane domains. *Mol. Microbiol.* 68:813–826.

3. Bryant, D. M., and K. E. Mostov. 2008. From cells to organs: building polarized tissue. *Nat. Rev. Mol. Cell Biol.* 9:887–901.

4. Bray, D. 2000. Cell Movements: From Molecules to Motility. Routledge, Abingdon, UK.

5. Blanchoin, L., R. Boujemaa-Paterski, …, J. Plastino. 2014. Actin dynamics, architecture, and mechanics in cell motility. *Physiol. Rev.* 94:235–263.

6. Pollard, T. D., and J. A. Cooper. 2009. Actin, a central player in cell shape and movement. *Science.* 326:1208–1212.

7. Rendon, A., D. Jung, and V. Jancsik. 1990. Interaction of microtubules and microtubule-associated proteins (MAPs) with rat brain mitochondria. *Biochem. J.* 269:555–556.

8. Fu, C., D. Jain, …, P. T. Tran. 2011. mmb1p binds mitochondria to dynamic microtubules. *Curr. Biol.* 21:1431–1439.

9. Waterman-Storer, C. M., and E. D. Salmon. 1998. Endoplasmic reticulum membrane tubules are distributed by microtubules in living cells using three distinct mechanisms. *Curr. Biol.* 8:798–806.

10. McIntosh, J. R., M. I. Molodtsov, and F. I. Ataullakhanov. 2012. Biophysics of mitosis. *Q. Rev. Biophys.* 45:147–207.

11. Tseng, Y., T. P. Kole, …, D. Wirtz. 2005. How actin crosslinking and bundling proteins cooperate to generate an enhanced cell mechanical response. *Biochem. Biophys. Res. Commun.* 334:183–192.

12. Loïodice, I., J. Staub, …, P. T. Tran. 2005. Ase1p organizes antiparallel microtubule arrays during interphase and mitosis in fission yeast. *Mol. Biol. Cell.* 16:1756–1768.

13. Janson, M. E., R. Loughlin, …, P. T. Tran. 2007. Crosslinkers and motors organize dynamic microtubules to form stable bipolar arrays in fission yeast. *Cell.* 128:357–368.

14. Subramanian, R., E. M. Wilson-Kubalek, …, T. M. Kapoor. 2010. Insights into antiparallel microtubule crosslinking by PRC1, a conserved nonmotor microtubule binding protein. *Cell.* 142:433–443.

15. Tulin, A., S. McClerklin, …, R. Dixit. 2012. Single-molecule analysis of the microtubule cross-linking protein MAP65-1 reveals a molecular mechanism for contact-angle-dependent microtubule bundling. *Biophys. J.* 102:802–809.

16. Stoppin-Mellet, V., V. Fache, …, M. Vantard. 2013. MAP65 coordinate microtubule growth during bundle formation. *PLoS One.* 8:e56808.

17. Lansky, Z., M. Braun, …, S. Diez. 2015. Diffusible crosslinkers generate directed forces in microtubule networks. *Cell.* 160:1159–1168.

18. Kellogg, E. H., S. Howes, …, E. Nogales. 2016. Near-atomic cryo-EM structure of PRC1 bound to the microtubule. *Proc. Natl. Acad. Sci. U S A.* 113:9430–9439.

19. Desai, A., and T. J. Mitchison. 1997. Microtubule polymerization dynamics. *Annu. Rev. Cell Dev. Biol.* 13:83–117.

20. dos Remedios, C. G., D. Chhabra, …, N. J. Nosworthy. 2003. Actin binding proteins: regulation of cytoskeletal microfilaments. *Physiol. Rev.* 83:433–473.

21. Kuan, H. S., and M. D. Betterton. 2013. Biophysics of filament length regulation by molecular motors. *Phys. Biol.* 10:036004.

22. Mohapatra, L., B. L. Goode, …, J. Kondev. 2016. Design principles of length control of cytoskeletal structures. *Annu. Rev. Biophys.* 45:85–116.

23. Pollard, T. D. 2016. Actin and actin-binding proteins. *Cold Spring Harb. Perspect. Biol.* 8:a018226.

24. Allard, J., and A. Mogilner. 2013. Traveling waves in actin dynamics and cell motility. *Curr. Opin. Cell Biol.* 25:107–115.

25. Barnhart, E. L., J. Allard, …, A. Mogilner. 2017. Adhesion-dependent wave generation in crawling cells. *Curr. Biol.* 27:27–38.

26. Dixit, R., and R. Cyr. 2004. Encounters between dynamic cortical microtubules promote ordering of the cortical array through angle-dependent modifications of microtubule behavior. *Plant Cell.* 16:3274–3284.

27. Allard, J. F., J. C. Ambrose, …, E. N. Cytrynbaum. 2010. A mechanochemical model explains interactions between cortical microtubules in plants. *Biophys. J.* 99:1082–1090.

28. Eren, E. C., R. Dixit, and N. Gautam. 2010. A three-dimensional computer simulation model reveals the mechanisms for self-organization of plant cortical microtubules into oblique arrays. *Mol. Biol. Cell.* 21:2674–2684.

29. Eren, E. C., N. Gautam, and R. Dixit. 2012. Computer simulation and mathematical models of the noncentrosomal plant cortical microtubule cytoskeleton. *Cytoskeleton (Hoboken).* 69:144–154.

30. Mogilner, A., and E. Craig. 2010. Towards a quantitative understanding of mitotic spindle assembly and mechanics. *J. Cell Sci.* 123:3435–3445.

31. Civelekoglu-Scholey, G., and D. Cimini. 2014. Modelling chromosome dynamics in mitosis: a historical perspective on models of metaphase and anaphase in eukaryotic cells. *Interface Focus.* 4:20130073.

32. Akamatsu, M., J. Berro, …, T. D. Pollard. 2014. Cytokinetic nodes in fission yeast arise from two distinct types of nodes that merge during interphase. *J. Cell Biol.* 204:977–988.

33. Stachowiak, M. R., C. Laplante, …, B. O'Shaughnessy. 2014. Mechanism of cytokinetic contractile ring constriction in fission yeast. *Dev. Cell.* 29:547–561.

34. Huxley, A. F. 1957. Muscle structure and theories of contraction. *Prog. Biophys. Biophys. Chem.* 7:255–318.

35. Huxley, A. F., and S. Tideswell. 1996. Filament compliance and tension transients in muscle. *J. Muscle Res. Cell Motil.* 17:507–511.

36. Huxley, A. F., and S. Tideswell. 1997. Rapid regeneration of power stroke in contracting muscle by attachment of second myosin head. *J. Muscle Res. Cell Motil.* 18:111–114.

37. Gardner, M. K., C. G. Pearson, …, D. J. Odde. 2005. Tension-dependent regulation of microtubule dynamics at kinetochores can explain metaphase congression in yeast. *Mol. Biol. Cell.* 16:3764–3775.

38. Gardner, M. K., D. J. Odde, and K. Bloom. 2008. Kinesin-8 molecular motors: putting the brakes on chromosome oscillations. *Trends Cell Biol.* 18:307–310.

39. Chacón, J. M., S. Mukherjee, …, M. K. Gardner. 2014. Pericentromere tension is self-regulated by spindle structure in metaphase. *J. Cell Biol.* 205:313–324.

40. Hepperla, A. J., P. T. Willey, …, M. K. Gardner. 2014. Minus-end-directed Kinesin-14 motors align antiparallel microtubules to control metaphase spindle length. *Dev. Cell.* 31:61–72.

41. Ward, J. J., H. Roque, …, F. Nédélec. 2014. Mechanical design principles of a mitotic spindle. *eLife.* 3:e03398.

42. Cytrynbaum, E. N., J. M. Scholey, and A. Mogilner. 2003. A force balance model of early spindle pole separation in Drosophila embryos. *Biophys. J.* 84:757–769.

43. Cytrynbaum, E. N., P. Sommi, …, A. Mogilner. 2005. Early spindle assembly in Drosophila embryos: role of a force balance involving cytoskeletal dynamics and nuclear mechanics. *Mol. Biol. Cell.* 16:4967–4981.

44. Wollman, R., G. Civelekoglu-Scholey, …, A. Mogilner. 2008. Reverse engineering of force integration during mitosis in the Drosophila embryo. *Mol. Syst. Biol.* 4:195.

45. Civelekoglu-Scholey, G., and J. M. Scholey. 2010. Mitotic force generators and chromosome segregation. *Cell. Mol. Life Sci.* 67:2231–2250.

46. Taylor, E. W. 1959. Dynamics of spindle formation and its inhibition by chemicals. *J. Biophys. Biochem. Cytol.* 6:193–196.

47. Hagan, I., and M. Yanagida. 1990. Novel potential mitotic motor protein encoded by the fission yeast cut7+ gene. *Nature.* 347:563–566.

48. Hagan, I., and M. Yanagida. 1992. Kinesin-related cut7 protein associates with mitotic and meiotic spindles in fission yeast. *Nature.* 356:74–76.

49. Ding, R., K. L. McDonald, and J. R. McIntosh. 1993. Three-dimensional reconstruction and analysis of mitotic spindles from the yeast, *Schizosaccharomyces pombe. J. Cell Biol.* 120:141–151.

50. Blackwell, R., C. Edelmaier, …, M. D. Betterton. 2017. Physical determinants of bipolar mitotic spindle assembly and stability in fission yeast. *Sci. Adv.* 3:e1601603.

51. Rincon, S. A., A. Lamson, …, P. T. Tran. 2017. Kinesin-5-independent mitotic spindle assembly requires the antiparallel microtubule crosslinker Ase1 in fission yeast. *Nat. Commun.* 8:15286.

52. Enos, A. P., and N. R. Morris. 1990. Mutation of a gene that encodes a kinesin-like protein blocks nuclear division in A. nidulans. *Cell.* 60:1019–1027.

53. Pidoux, A. L., M. LeDizet, and W. Z. Cande. 1996. Fission yeast pkl1 is a kinesin-related protein involved in mitotic spindle function. *Mol. Biol. Cell.* 7:1639–1655.

54. Cochran, J. C., C. A. Sontag, …, S. P. Gilbert. 2004. Mechanistic analysis of the mitotic kinesin Eg5. *J. Biol. Chem.* 279:38861–38870.

55. Yamashita, A., M. Sato, …, T. Toda. 2005. The roles of fission yeast ase1 in mitotic cell division, meiotic nuclear oscillation, and cytokinesis checkpoint signaling. *Mol. Biol. Cell.* 16:1378–1395.

56. Valentine, M. T., P. M. Fordyce, …, S. M. Block. 2006. Individual dimers of the mitotic kinesin motor Eg5 step processively and support substantial loads in vitro. *Nat. Cell Biol.* 8:470–476.

57. Bratman, S. V., and F. Chang. 2007. Stabilization of overlapping microtubules by fission yeast CLASP. *Dev. Cell.* 13:812–827.

58. Braun, M., Z. Lansky, …, M. E. Janson. 2011. Adaptive braking by Ase1 prevents overlapping microtubules from sliding completely apart. *Nat. Cell Biol.* 13:1259–1264.

59. Chen, C. J., K. Porche, …, S. P. Gilbert. 2012. The ATPase pathway that drives the kinesin-14 Kar3Vik1 powerstroke. *J. Biol. Chem.* 287:36673–36682.

60. Edamatsu, M. 2014. Bidirectional motility of the fission yeast kinesin-5, Cut7. *Biochem. Biophys. Res. Commun.* 446:231–234.

61. Britto, M., A. Goulet, …, R. A. Cross. 2016. Schizosaccharomyces pombe kinesin-5 switches direction using a steric blocking mechanism. *Proc. Natl. Acad. Sci. U S A.* 113:E7483–E7489.

62. Novak, M., B. Polak, …, N. Pavin. 2018. The mitotic spindle is chiral due to torques within microtubule bundles. *Nat. Commun.* 9:3571.

63. Yukawa, M., Y. Yamada, …, T. Toda. 2018. Two spatially distinct Kinesin-14 proteins, Pkl1 and Klp2, generate collaborative inward forces against Kinesin-5 Cut7 in S. pombe. *J Cell Sci.* 131::jcs210740.

64. Hoyt, M. A., L. He, …, W. S. Saunders. 1992. Two *Saccharomyces cerevisiae* kinesin-related gene products required for mitotic spindle assembly. *J. Cell Biol.* 118:109–120.

65. Sawin, K. E., K. LeGuellec, …, T. J. Mitchison. 1992. Mitotic spindle organization by a plus-end-directed microtubule motor. *Nature.* 359:540–543.

66. Blangy, A., H. A. Lane, …, E. A. Nigg. 1995. Phosphorylation by p34cdc2 regulates spindle association of human Eg5, a kinesin-related motor essential for bipolar spindle formation in vivo. *Cell.* 83:1159–1169.

67. Mayer, T. U., T. M. Kapoor, …, T. J. Mitchison. 1999. Small molecule inhibitor of mitotic spindle bipolarity identified in a phenotype-based screen. *Science.* 286:971–974.

68. Sharp, D. J., K. R. Yu, …, J. M. Scholey. 1999. Antagonistic microtubule-sliding motors position mitotic centrosomes in Drosophila early embryos. *Nat. Cell Biol.* 1:51–54.

69. Goshima, G., and R. D. Vale. 2003. The roles of microtubule-based motor proteins in mitosis: comprehensive RNAi analysis in the Drosophila S2 cell line. *J. Cell Biol.* 162:1003–1016.

70. Waitzman, J. S., and S. E. Rice. 2014. Mechanism and regulation of kinesin-5, an essential motor for the mitotic spindle. *Biol. Cell.* 106:1–12.

71. Troxell, C. L., M. A. Sweezy, …, J. R. McIntosh. 2001. Pkl1 +andklp2 +: two kinesins of the Kar3 Subfamily in fission yeast Perform different functions in both mitosis and meiosis. *Mol. Biol. Cell.* 12:3476–3488.

72. Olmsted, Z. T., A. G. Colliver, …, J. L. Paluh. 2014. Kinesin-14 and kinesin-5 antagonistically regulate microtubule nucleation by γ-TuRC in yeast and human cells. *Nat. Commun.* 5:5339.

73. Prelogović, M., L. Winters, …, N. Pavin. 2017. Pivot-and-bond model explains microtubule bundle formation. *bioRxiv* https://doi.org/10.1101/157719.

74. Winters, L., I. Ban, …, I. M. Tolic. 2018. Pivoting of microtubules driven by minus end directed motors leads to their alignment to form an interpolar bundle. *bioRxiv* https://doi.org/10.1101/347831.

75. Kalinina, I., A. Nandi, …, I. M. Tolić-Norrelykke. 2013. Pivoting of microtubules around the spindle pole accelerates kinetochore capture. *Nat. Cell Biol.* 15:82–87, Published online December 9, 2012.

76. Blackwell, R., O. Sweezy-Schindler, …, M. D. Betterton. 2017. Contributions of microtubule dynamic instability and rotational diffusion to kinetochore capture. *Biophys. J.* 112:552–563.

77. Laan, L., N. Pavin, …, M. Dogterom. 2012. Cortical dynein controls microtubule dynamics to generate pulling forces that position microtubule asters. *Cell.* 148:502–514.

78. Pavin, N., L. Laan, …, F. Jülicher. 2012. Positioning of microtubule organizing centers by cortical pushing and pulling forces. *New J. Phys.* 14:105025.

79. Ma, R., L. Laan, …, F. Jülicher. 2014. General theory for the mechanics of confined microtubule asters. *New J. Phys.* 16:013018.

80. Dogterom, M., and S. Leibler. 1993. Physical aspects of the growth and regulation of microtubule structures. *Phys. Rev. Lett.* 70:1347–1350.

81. Redemann, S., J. Baumgart, …, T. Müller-Reichert. 2017. C. elegans chromosomes connect to centrosomes by anchoring into the spindle network. *Nat. Commun.* 8:15288.

82. Bratman, S. V., and F. Chang. 2008. Mechanisms for maintaining microtubule bundles. *Trends Cell Biol.* 18:580–586.

83. McIntosh, J. R., Z. Cande, …, K. Vanderslice. 1975. Studies on the mechanism of mitosis. *Ann. N. Y. Acad. Sci.* 253:407–427.

84. McIntosh, J. R., K. L. McDonald, …, B. M. Ross. 1979. Three-dimensional structure of the central mitotic spindle of Diatoma vulgare. *J. Cell Biol.* 83:428–442.

85. McIntosh, J. R., U. P. Roos, …, K. L. McDonald. 1985. Architecture of the microtubule component of mitotic spindles from *Dictyostelium discoideum. J. Cell Sci.* 75:93–129.

86. Winey, M., C. L. Mamay, …, J. R. McIntosh. 1995. Three-dimensional ultrastructural analysis of the *Saccharomyces cerevisiae* mitotic spindle. *J. Cell Biol.* 129:1601–1615.

87. Dogterom, M., and B. Yurke. 1997. Measurement of the force-velocity relation for growing microtubules. *Science.* 278:856–860.

88. Kikumoto, M., M. Kurachi, …, H. Tashiro. 2006. Flexural rigidity of individual microtubules measured by a buckling force with optical traps. *Biophys. J.* 90:1687–1696.

89. Mercedes Tirado, M., C. L. Martínez, and J. García de la Torre. 1984. Comparison of theories for the translational and rotational diffusion coefficients of rod-like macromolecules. Application to short DNA fragments. *J. Chem. Phys.* 81:2047–2052.

90. Grishchuk, E. L., and J. R. McIntosh. 2006. Microtubule depolymerization can drive poleward chromosome motion in fission yeast. *EMBO J.* 25:4888–4896.

91. Subramanian, R., S. C. Ti, …, T. M. Kapoor. 2013. Marking and measuring single microtubules by PRC1 and kinesin-4. *Cell.* 154:377–390.

92. Kashina, A. S., R. J. Baskin, …, J. M. Scholey. 1996. A bipolar kinesin. *Nature.* 379:270–272.

93. Pringle, J., A. Muthukumar, …, J. L. Ross. 2013. Microtubule organization by kinesin motors and microtubule crosslinking protein MAP65. *J. Phys. Condens. Matter.* 25:374103.

94. Flory, M. R., M. Morphew, …, T. N. Davis. 2002. Pcp1p, an Spc110p-related calmodulin target at the centrosome of the fission yeast *Schizosaccharomyces pombe. Cell Growth Differ.* 13:47–58.

95. Muller, E. G., B. E. Snydsman, …, T. N. Davis. 2005. The organization of the core proteins of the yeast spindle pole body. *Mol. Biol. Cell.* 16:3341–3352.

96. Derényi, I., F. Jülicher, and J. Prost. 2002. Formation and interaction of membrane tubes. *Phys. Rev. Lett.* 88:238101.

97. Alberts, B., A. Johnson, …, P. Walter. 2008. Molecular Biology of the Cell, Fifth edition. Garland Science, New York.

98. Janson, M. E., M. E. de Dood, and M. Dogterom. 2003. Dynamic instability of microtubules is regulated by force. *J. Cell Biol.* 161:1029–1034.

99. Lim H W, G., G. Huber, …, S. Sazer. 2007. Vesicle-like biomechanics governs important aspects of nuclear geometry in fission yeast. *PLoS One.* 2:e948.

100. Carpy, A., K. Krug, …, B. Macek. 2014. Absolute proteome and phosphoproteome dynamics during the cell cycle of *Schizosaccharomyces pombe* (Fission Yeast). *Mol. Cell. Proteomics.* 13:1925–1936.

101. Bancaud, A., S. Huet, …, J. Ellenberg. 2009. Molecular crowding affects diffusion and binding of nuclear proteins in heterochromatin and reveals the fractal organization of chromatin. *EMBO J.* 28:3785–3798.

102. Kapitein, L. C., M. E. Janson, …, E. J. Peterman. 2008. Microtubule-driven multimerization recruits ase1p onto overlapping microtubules. *Curr. Biol.* 18:1713–1717.